Comprehensive Analysis and Wide Range Operation of ZVS and Quasi-ZPA in Wireless Power Transfer System

Xian Zhang, Zhenlei Zhang, Fei Xu, *Member, IEEE*, and Zhixin Chen, *Graduate Student Member, IEEE*

***Abstract*—To reduce switching loss and minimize backflow power, zero voltage switching (ZVS) and zero phase angle (ZPA) technology are normally implemented in wireless power transfer (WPT) systems. However, traditional concepts of ZPA and ZVS are usually independent and misleading, lacking clear and strict theoretical explanations. More importantly, the design of ZPA circuit parameters is usually based on fundamental harmonic analysis in the frequency domain. To tackle this problem, first, comprehensive analysis of the relationships among ZVS, ZPA, and quasi-ZPA (time-domain) are discussed in detail. Second, an impedance factor δ based on multiharmonic analysis is proposed to evaluate the input current characteristics of WPT systems under different topologies and load conditions. Third, δ is associated with quasi-ZPA, and the boundary value δ_{th} required to achieve quasi-ZPA is defined. Finally, an experimental prototype with $1\,\mathrm{kW}/85\,\mathrm{kHz}$ is built to verify the analysis. Experimental results demonstrate that the impedance factor δ proposed is consistent with the theoretical analysis regarding its influence on the input current waveform characteristics of the WPT system. In addition, phase shift control enables constant power output and ZVS across a wide load range.**

***Index Terms*—Impedance factor, multiple harmonics analysis (MHA), quasi-ZPA, zero phase angle (ZPA), zero voltage switching (ZVS).**

I. Introduction

With the rapid advancement of technology, wireless power transfer (WPT) has become a significant branch in the modern electronics field [1], [2]. Inductive power transfer (IPT) as a short-range WPT technology utilizes the high-frequency magnetic field to achieve a wireless energy transfer between transmitting and receiving coils. Compared to traditional wired power transfer, IPT offers advantages, such as greater flexibility, safety, reliability, and convenience. Its applications have expanded from simple consumer electronics to more complex fields, including industrial systems [3], implantable biomedical devices [4], [5], autonomous underwater vehicle [6], and electric vehicle charging [7], [8], [9].

The essence of IPT technology lies in achieving efficient and safe energy transmission without relying on physical contact. In this field, zero phase angle (ZPA) and zero voltage switching (ZVS) technologies have gained significant attention due to their remarkable advantages in enhancing system efficiency and reducing switching losses. ZPA technology refers to the design of specific compensation network parameters in a wireless power transfer system to ensure that the system operates in a resonant state under the influence of the voltage fundamental wave, making the input impedance purely resistive. ZPA design optimizes power transfer efficiency and minimizes power loss caused by impedance mismatching. In contrast, ZVS technology [10] involves a control strategy in power supplies or inverters, where the switching device operates when the voltage is zero. This approach eliminates switching losses and electromagnetic interference, thereby improving the overall efficiency of the system.

Circuit analysis for resonant converter topology design and system parameter optimization is normally based on fundamental harmonic analysis (FHA) [11], [12]. The FHA is favored in circuit analysis for two main reasons: 1) It is relatively simpler compared to time-domain analysis and 2) it transforms the circuit model from a complex time-domain representation to the frequency-domain, considering only the first harmonic as the input source, while neglecting higher order harmonics, thus significantly simplifying the analysis. This approach is also beneficial for the equivalent calculation of rectifier circuits. Under the first harmonic approximation, rectifier networks, filter capacitors, and loads can be modeled as resistances [13], [14], [15]. As a result, FHA is highly convenient for use in IPT systems. However, applying first harmonic analysis to different topologies results in a purely resistive input impedance, which may not accurately reflect the impedance characteristics of the system. The accuracy of FHA depends on the topology and parameter settings of the circuit, as circuit waveforms can vary with these factors. The primary cause of this discrepancy is total harmonic distortion (THD), which introduces analysis errors

Received 5 March 2025; revised 5 June 2025 and 14 July 2025; accepted 7 August 2025. Date of publication 12 August 2025; date of current version 22 October 2025. This work was supported in part by the China National Foundation Project under Grant 52477005 and Grant 52407004, in part by the Key Program of Natural Science Foundation of Tianjin under Grant 22JCZDJC00620, in part by the Hebei Yanzhao Golden Platform Talent Gathering Plan Backbone Talent Project (Study Abroad Return Platform) under Grant A2025003, in part by the Hebei Province Yout Talent Program under Grant BJK2024059, in part by the Hebei Yanzhao Young Scientist Project under Grant E2024202109, and in part by the the S&T Program of Hebei under Grant 24464401D. Recommended for publication by Associate Editor S. Mekhilef. *(Corresponding author: Fei Xu.)*

The authors are with the State Key Laboratory of Intelligent Power Distribution Equipment and System, Hebei University of Technology, Tianjin 300401, China, and also with the Hebei Key Laboratory of Equipment and Technology Demonstration of Flexible DC Transmission, Hebei University of Technology, Tianjin 300401, China (e-mail: zhangxian@hebut.edu.cn; 202331402130@hebut.edu.cn; feify.xu@connect.polyu.hk; zhixinchen@ieee.org).

Color versions of one or more figures in this article are available at https://doi.org/10.1109/TPEL.2025.3598146.

Digital Object Identifier 10.1109/TPEL.2025.3598146

between theoretical and practical results. The accuracy of FHA varies with the system's THD, with lower THD resulting in higher accuracy. The omission of higher order harmonics leads to the neglect of the inductive effects caused by the rectifier network, filter capacitors, and loads, which can lead to design deviations in the compensation network [16], [17], [18], [19], [20].

However, FHA can only achieve ZPA performance for some certain resonant topologies, such as the SS topology. However, for some other topologies, such as the LCC–LCC topology [21], it cannot achieve satisfactory ZPA. In addition, the system would generate backflow power if the operating conditions of ZPA are designed with a large margin. The amount of backflow power impacts the overall transmission efficiency of the IPT system [22], [23]. To address these limitations and improve performance, phase shift control can be applied to achieve constant power output and ZVS over a wide load range, helping to optimize the performance of the wireless power transfer system [10], [20], [24].

Therefore, it is essential to distinguish between quasi-ZPA in the time-domain and ZPA in the frequency-domain. Moreover, even after configuring resonant parameters through first harmonic analysis for different topologies, achieving ZPA is not always guaranteed.

To tackle this problem, this article focuses on conducting multiple harmonics analysis (MHA) for various IPT topologies and introduces a novel concept named the impedance factor. The impedance factor is used to study and compare current conditions under different topologies and operating scenarios, establishing a connection between harmonic impedance and fundamental impedance. The parameter δ represents the relative value of higher order harmonic impedance, with its magnitude reflecting the quasi-ZPA and ZVS conditions of the input current waveform under different topologies, resonance parameters, and operating scenarios. A larger δ corresponds to lower system backflow power and a dominant fundamental harmonic, making the waveform closer to a sinusoidal shape, enabling the topology to achieve quasi-ZPA.

The main contributions of this article are as follows.

1) Comprehensive analysis of the relationships among ZPA, ZVS, and the phenomenon where using FHA to configure parameters results in the system achieving ZVS is presented. The concept of quasi-ZPA is introduced, linking small backflow power with ZVS. In addition, the impedance factor, denoted as δ, is introduced, and its effect on ZVS and quasi-ZPA under varying values is analyzed.
2) A detailed analysis of the mechanism of harmonic impedance in the circuit is conducted, deriving the general expression for the input impedance at each harmonic. The influence of harmonic impedance from different topologies on the input current characteristics is analyzed, and the relationship between the value of δ and topology parameters is studied. Based on this, δ_{th} is identified as the boundary for achieving quasi-ZPA in the system. The results show that for different topologies, resonant parameters, and operating conditions, the input current characteristics can be determined simply by comparing the calculated value of δ with the threshold δ_{th}.

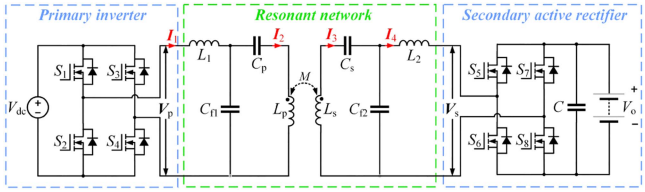

Fig. 1. Simplest LCC–LCC compensation IPT topology with active rectifier.

The rest of this article is organized as follows. In Section II, multiharmonic circuit model is used for various IPT topologies, and the general expression for input impedance under MHA is derived. Based on this, the concept of the impedance factor δ is introduced, and the relationship between quasi-ZPA and δ is defined. In Section III, based on the LCC–LCC topology, a full-bridge active rectifier control strategy is implemented on the secondary side, and the relationships between internal and external phase shifts and output power are derived to achieve ZVS and quasi-ZPA simultaneously. In Section IV, simulation are conducted to verify the theoretical analysis. In Section V, multiple topological experimental platforms are built to verify variation laws under different load conditions. Finally, Section VI concludes this article.

II. Analysis of MHA Model in IPT System

In IPT systems, the FHA is predominantly utilized. Because FHA only considers the fundamental wave, the calculated equivalent impedance at the fundamental wave $Z_{\text{eq(1)}}$ is purely resistive, thereby minimizing losses. However, this approach can be influenced by harmonics and different load conditions in certain topologies, leading to analysis inaccuracies. In addition, the traditional ZPA is defined in the frequency domain. Therefore, the ZPA obtained by modeling with FHA is only valid under the action of the fundamental wave and is not actually a ZPA in the time domain. Consequently, harmonics should be taken into account to conduct a relatively comprehensive analysis of the traditional ZPA and ZVS by using MHA.

A. LCC–LCC Compensation Model Based on FHA

Fig. 1 shows the typical LCC–LCC compensation IPT topology with a secondary active rectifier and battery load. For the convenience of reference, the subscripts "p" and "s" represent the parameters of the primary side and the secondary side, respectively. The typical LCC–LCC compensation IPT topology has self-inductances L_1, L_2, L_{p}, L_{s}, and mutual inductance M, and the coupling coefficient is given by $k = M/\sqrt{L_{\text{p}}L_{\text{s}}}$. The compensation capacitors C_{p}, C_{f1}, C_{s}, and C_{f2} are driven by the primary inverter with a high frequency voltage V_{p} and the secondary active rectifier with a high frequency voltage V_{s}.

The inverter is powered by the dc power supply V_{dc} and contains two sets of H-bridge circuits composed of S_1–S_8. One of them generates the high frequency voltage V_{p}, and the other, which is located on the secondary side, serves as a full bridge rectifier circuit to output V_{o}. Here, S_1–S_8 are MOSFETs, and each MOSFET has its own body diode, respectively.

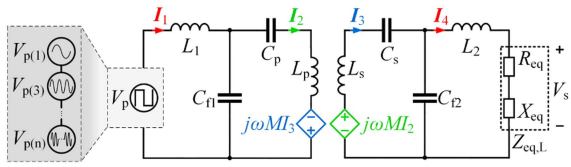

Fig. 2. Equivalent circuit of the magnetic coupler of Fig. 1.

Designing parameters for LCC–LCC topology by using FHA requires making C_p, C_{f1}, C_s, aand C_{f1} in the system compensate for L_1, L_2, L_p, and L_s to match the required resonant frequency f. The aim is to achieve impedance matching and enhance IPT efficiency. The operating switching frequency is usually designed at the resonant frequency, i.e.,

$$\omega = \frac{1}{\sqrt{L_1 C_{fl}}} = \frac{1}{\sqrt{L_2 C_{f2}}} = \frac{1}{\sqrt{(L_p - L_1)C_p}} = \frac{1}{\sqrt{(L_s - L_2)C_s}}. \tag{1}$$

Fig. 2 shows the equivalent circuit of the LCC–LCC topology, and the expression for the output voltage V_p passing through the primary inverter with a high frequency, i.e.,

$$V_p = \begin{cases} V_{dc}, & t \in \left[kT, (2k+1)\frac{T}{2}\right] \\ -V_{dc}, & t \in \left((2k+1)\frac{T}{2}, (k+1)T\right]. \end{cases} \tag{2}$$

The high-frequency voltage V_p can be obtained through Fourier series expansion as follows:

$$V_p = \frac{4V_{dc}}{\pi} \sum_{n=1}^{k} \frac{1}{n} \sin n\omega t \quad (k = 1, 3, 5 \cdots). \tag{3}$$

Under the influence of the fundamental wave alone, when parameter tuning is performed based on FHA, the LCC–LCC topology generally exhibits a purely resistive behavior. When the excitation source is a square wave input, the influence of harmonics causes the system's input impedance to become inductive under the parameter configuration modeled by FHA. The system can achieve natural ZVS. However, the backflow power of the system will change accordingly due to variations in topology and load. While ZVS can be achieved, it may result in a reduction in system efficiency.

B. LCC–LCC Harmonic Compensation Model

After the output voltage of the inverter is decomposed by Fourier, apart from the fundamental wave, it also contains numerous harmonic components. In the LCC–LCC compensation network, L_1 and C_{f1} constitute a low-pass filter. This filter effectively eliminates the high-order harmonic components in the transmitting coil, so that the primary side current almost solely consists of the fundamental wave component. However, the current flowing through L_1 contains a large number of harmonic components, and the system will generate uncontrollable backflow power. Hence, an analysis on the harmonics is conducted.

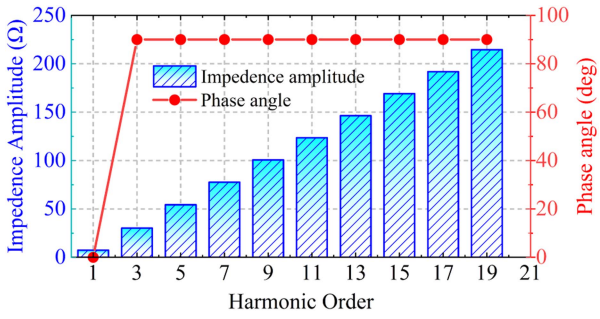

Fig. 3. Phase angle and impedance magnitude under different harmonic orders from LCC–LCC Topology.

To simplify the theoretical analysis, it is assumed that the equivalent series impedances of all compensation networks can be neglected. Using Fourier analysis, the high-frequency voltage V_p is decomposed into its fundamental wave and a series of harmonic components. When each harmonic is regarded as an excitation source separately, the loop equations can be listed as shown in (4) shown at the bottom of this page.

When the nth harmonic is taken as the excitation source, the equivalent input impedance is solved as

$$Z_{eq(n)} = \frac{C + Dj}{E + Fj} \tag{5}$$

where the variables are shown in

$$\begin{cases} A &= n\omega \\ B &= \frac{\omega}{n} \\ C &= L_1 L_2 \left(B^2 L_1 - (A-B)^2 L_p\right)\left((A-B)^2 L_s - B^2 L_2\right) \\ &\quad + A^2 L_1 L_2 (A-B)^2 M^2 \\ D &= (A-B)\left(-2AB L_p L_s + B^2(-L_1 + L_p)L_s \right. \\ &\quad \left. + A^2(L_p L_s - M^2)\right) L_1 R_{eq} \\ E &= \left((A-B)^2 L_p L_s - A^2 M^2\right) R_{eq} \\ F &= (A-B)\left((A-B)^2 L_p L_s - B^2 L_p L_2 - A^2 M^2\right) L_2. \end{cases} \tag{6}$$

From (5) and (6), the variation of phase angle and impedance magnitude of LCC–LCC topology under different harmonic orders can be derived. The curves of the phase angle and impedance magnitude for both the fundamental wave and harmonic components versus harmonic order are plotted in Fig. 3.

$$\begin{cases} V_p &= j(n\omega)L_1 I_1 + \frac{1}{j(n\omega)C_{f1}} I_1 - \frac{1}{j(n\omega)C_{f1}} I_2 \\ 0 &= -\frac{1}{j(n\omega)C_{f1}} I_1 + \left[\frac{1}{j(n\omega)C_{f1}} + \frac{1}{j(n\omega)C_p} + j(n\omega)L_p\right] I_2 - j(n\omega)M I_3 \\ 0 &= -j(n\omega)M I_2 + \left[\frac{1}{j(n\omega)C_s} + \frac{1}{j(n\omega)C_{f1}} + j(n\omega)L_s\right] I_3 - \frac{1}{j(n\omega)C_{f1}} I_4 \\ 0 &= -\frac{1}{j(n\omega)C_{f1}} I_3 + \left[\frac{1}{j(n\omega)C_{f1}} + j(n\omega)L_2 + R_{eq}\right] I_4. \end{cases} \tag{4}$$

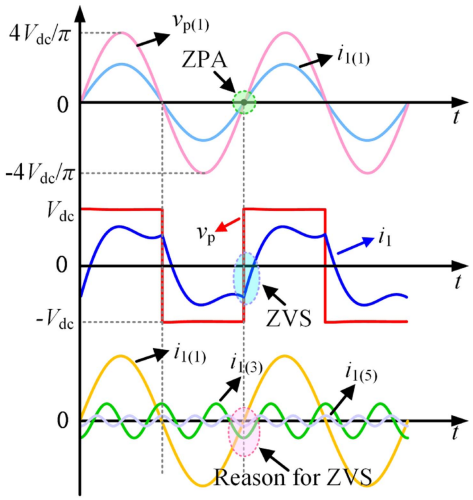

Fig. 4. Explanation of ZPA and ZVS Waveforms.

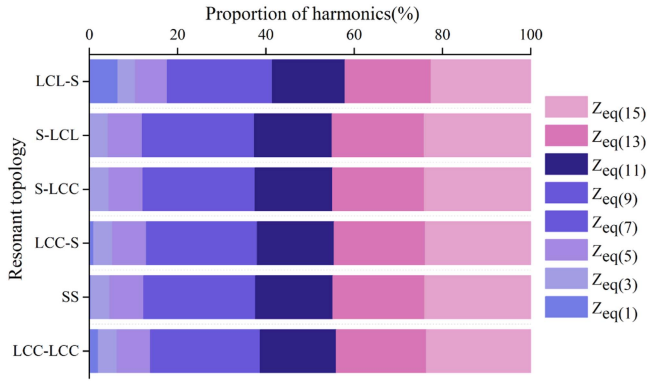

Fig. 5. Harmonic impedance proportion of different topologies.

As shown in Fig. 3, when the fundamental wave acts, the input impedance of the system is purely resistive; when the harmonics act, the input impedance is purely inductive. Moreover, the higher the harmonic order, the larger the impedance becomes, resulting in a smaller harmonic current.

C. Analysis of the Causes of System Natural ZVS

Fourier decomposition is performed on V_{p} shown in Fig. 2, dividing it into a fundamental wave source and individual harmonic sources. The currents generated by the individual actions of the fundamental wave and each harmonic are analyzed.

Fig. 4 shows the output current waveform of the inverter under a square-wave voltage input. The analysis of ZPA and ZVS is established from two different perspectives: The frequency domain and the time domain. 1) In the frequency domain, only the fundamental components of voltage and current are considered, as described by the FHA. Under this condition, ZPA can be achieved through proper parameter configuration. This approach provides a convenient basis for initial parameter design. 2) In the time domain, however, the system exhibits significant harmonic impedance and inductive impedance angles due to the square-wave input. Through time-domain analysis, such as MHA, it is observed that the system is capable of achieving ZVS. Nevertheless, backflow power is inevitably introduced. Since the magnitude of backflow power is highly sensitive to the load, parameter settings, and circuit topology, it becomes difficult to control.

D. Effect of Load Changes in Diverse Topologies on Backflow Power

To analyze the influence of different topologies on harmonic effects, several commonly used WPT system topologies are selected for theoretical analysis, including SS, LCC-S, S-LCC, LCL-S, S-LCL, and LCC-LCC, all of which have resonant conditions that depend only on their own parameters. The resonant conditions for each topology are derived using the FHA method, and the harmonic input impedance for different harmonic orders is calculated. The results are presented in Table I, which shows the relationship between harmonic input impedance and harmonic order.

Fig. 5 illustrates the proportion of input impedance under different harmonic orders for various topologies, obtained using FHA with a constant load of 10 Ω. Using the formulas in Table I, the phase angles of the input impedance for each topology under harmonic inputs, except for the fundamental wave, are all inductive. Therefore, their phase angles are not plotted in the illustration. Since the third harmonic impedance $Z_{\mathrm{eq}(3)}$ of the LCL-S topology is smaller than $Z_{\mathrm{eq}(k)}$ $(k \neq 3)$, this topology theoretically exhibits the smallest third harmonic impedance, resulting in its input current waveform being more significantly affected by harmonic currents and leading to increased backflow power. For the S-LCL, S-LCC, and SS topologies, $Z_{\mathrm{eq}(1)}$ is approximately 0 in proportion. Therefore, the waveforms of these topologies are dominated by the fundamental harmonic, with relatively small backflow power, and quasi-ZPA can be more readily achieved. For the LCC-S and LCC-LCC topologies, $Z_{\mathrm{eq}(1)}$ is larger in proportion compared with the above topologies. Therefore, the waveforms of these topologies are significantly affected by harmonics. In this case, ZVS is easily achieved, but the system will lose quasi-ZPA.

To analyze the influence of harmonic impedance under different load values, the impedance factor δ is defined as follows:

$$\delta = \log_{10}\left(\frac{\sqrt{\sum_{n=1,3,\ldots}^{\infty} Z_{\mathrm{eq}(n)}^2}}{Z_{\mathrm{eq}(1)}}\right). \tag{7}$$

Specifically, a larger value of δ indicates that the impedance of higher order harmonics is significantly greater than that of the fundamental component. In this case, the input current waveform is primarily composed of the fundamental harmonic, resulting in a waveform that is closer to an ideal sinusoid. This allows the system to achieve zero phase difference in the time domain (quasi-ZPA), with reduced distortion and lower backflow power. Conversely, a smaller value of δ reflects a stronger influence of harmonic components, leading to a more distorted waveform,

TABLE I
CALCULATION FORMULAS FOR THE HARMONIC IMPEDANCE OF EACH ORDER OF DIFFERENT TOPOLOGIES

References	Topology	Structure	Calculation Formulas for Input Impedance
[25]	SS	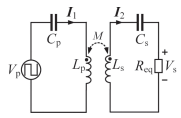	$C = L_pL_s(A-B)^2 - A^2M^2$ $D = (B-A)L_pR_{eq}$ $E = R_{eq}$ $F = (A-B)L_s$
[26]	LCL-S	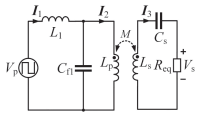	$C = A(B-A)L_p((A-2B)L_pL_s - AM^2)$ $D = (A-2B)L_p^2R_{eq}$ $E = (A-B)L_pR_{eq}$ $F = (A-B)^2L_pL_s - A^2M^2$
[29]	S-LCL	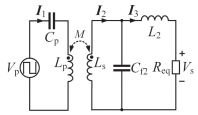	$C = A(A-B)L_p((A-2B)L_pL_s - AM^2)$ $D = (A^2M^2 - (A-B)^2L_pL_s)R_{eq}$ $E = (B-A)L_sR_{eq}$ $F = A(2B-A)L_s^2$
[27]	LCC-S	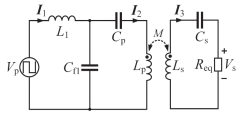	$C = (B-A)L_1((A-B)^2L_pL_s - B^2L_1L_s - A^2M^2)$ $D = ((A-B)^2L_p - B^2L_1)L_1R_{eq}$ $E = (A-B)L_pR_{eq}$ $F = (A-B)^2L_pL_s - A^2M^2$
[28]	S-LCC	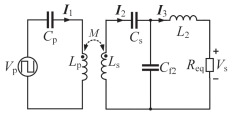	$C = (A-B)L_1((A-B)^2L_pL_s - B^2L_1L_p - A^2M^2))$ $D = (A^2M^2 - (A-B)^2L_pL_s)R_{eq}$ $E = (B-A)L_sR_{eq}$ $F = (B^2L_1 - (A-B)^2L_s)L_1$
[21]	LCC-LCC	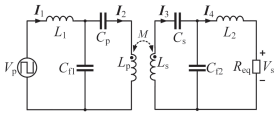	$C = L_1L_2(B^2L_1 - (A-B)^2L_p)((A-B)^2L_s - B^2L_2) + A^2L_1L_2(A-B)^2M^2$ $D = (A-B)(-2ABL_pL_s + B^2(-L_1+L_p)L_s + A^2(L_pL_s - M^2))L_1R_{eq}$ $E = ((A-B)^2L_pL_s - A^2M^2)R_{eq}$ $F = (A-B)((A-B)^2L_pL_s - B^2L_pL_2 - A^2M^2)L_2$

higher reverse power, and deviation from the quasi-ZPA operating condition. The influence of equivalent series resistance on the overall impedance is relatively minor and thus was not explicitly included in the δ calculation.

Through theoretical algebraic calculations, it is found that $Z_{eq(m)}$ $(m \neq 1)$ remains nearly constant, while δ reflects the variation trend of the fundamental current. A larger δ indicates a greater fundamental current. When the fundamental current is sufficiently large, the harmonic currents become relatively small, the system's total input voltage and current can thereby achieve quasi-ZPA. Therefore, there exists a threshold value δth, which serves as the boundary for whether the system can achieve quasi-ZPA. Theoretically, when the calculated value of δ is around 2.25, the third harmonic current is approximately one twenty-fourth of the fundamental current, and the third harmonic impedance is eight times the fundamental impedance. In this article, this value of δ is regarded as the critical threshold δ_{th} for achieving quasi-ZPA. When δ is less than δ_{th}, the smaller the value of δ, the more pronounced the harmonic effects become. Conversely, as δ gradually approaches and exceeds δ_{th}, the fundamental harmonic component dominates the waveform, making the influence of harmonics less noticeable. Considering that the phenomenon becomes less pronounced as δ approaches the threshold, the tolerance for δ is set to $\pm 5\%$ of δ_{th}. Therefore, the minimum value of δ for achieving quasi-ZPA in this study is defined as $0.95\ \delta_{th}$.

Fig. 6 shows the variation of the theoretical value of δ when the magnetic coupler is the same but the topologies and loads are

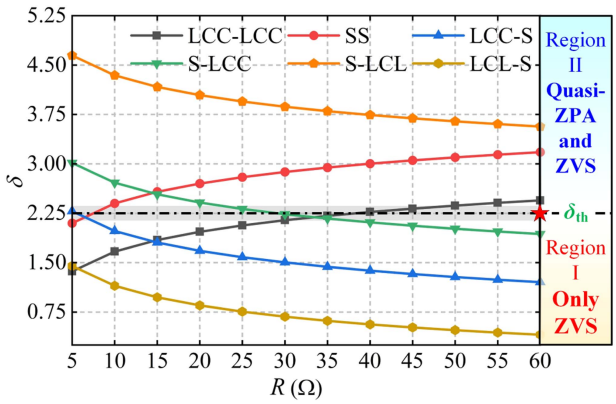

Fig. 6. Variation curve of δ with the load for different topologies.

different. According to the variation of δ in the figure, it can be concluded that for the SS and LCC-LCC topologies, as the load increases, δ also increases and gradually exceeds the threshold value δ_{th}. The input current will be increasingly dominated by the fundamental harmonic component, and the system will more easily achieve quasi-ZPA as the load increases. For the S-LCL topology, since its δ value is always much higher than δ_{th}, the fundamental current always dominates, and thus, the system can maintain quasi-ZPA regardless of the load variations. For the S-LCC and LCC-S topologies, as the load increases, the δ value will gradually fall below δ_{th}, indicating that the harmonic currents have a more significant influence, and the system will

gradually lose quasi-ZPA. For the LCL-S topology, its value is always below $\delta_{\rm th}$, so regardless of the load variations, the system will always be affected by harmonics, and as the load increases, the harmonic influence and backflow power will become more pronounced. As a result, the system will not achieve quasi-ZPA.

In summary, Fig. 6 is categorized into two regions and four distinct variation patterns based on the changes in δ, with each region illustrating how δ affects the characteristics of the input waveform. When operating in Region I, δ always remains below $\delta_{\rm th}$. If its value decreases further with increasing load, the harmonic effects in the system become more pronounced, resulting in a gradual increase in backflow power. Moreover, when operating in Region II, δ consistently exceeds $\delta_{\rm th}$, thereby enabling the system to continuously sustain the quasi-ZPA condition. Under these circumstances, the input current waveform remains predominantly determined by its fundamental harmonic component. During the transition from Region I to Region II, the system exhibits distinct operational characteristics. In Region I, with δ remaining below $\delta_{\rm th}$, the influence of harmonics is considerable, allowing only ZVS to be realized rather than quasi-ZPA. As δ increases and surpasses $\delta_{\rm th}$ into Region II, the input current waveform becomes predominantly determined by its fundamental harmonic component, thereby enabling the simultaneous achievement of both quasi-ZPA and ZVS. In contrast, during the transition from Region II to Region I, the system displays the reverse behavior. While operating in Region II, with δ exceeding $\delta_{\rm th}$, the input current waveform is dominated by the fundamental harmonic component, thereby enabling the realization of both quasi-ZPA and ZVS. However, as the system enters Region I and δ falls below $\delta_{\rm th}$, the increased influence of harmonics leads to the loss of quasi-ZPA, and only ZVS can be maintained. To further elucidate the influence of δ on the input current, representative input current variation characteristics are selected from Fig. 6 for analysis. The corresponding trends between δ and input current are illustrated in Fig. 7. Specifically, Fig. 7(a) presents the input current variation as δ increases from 1.36 to 2.36 in the LCC–LCC topology, corresponding to the transition from Region I to Region II. Fig. 7(b) depicts the trend as δ decreases from 1.44 to 0.47, representing the state where the system always operates in Region I. Fig. 7(c) shows the current variation as δ decreases from 3.01 to 1.81, corresponding to the transition from Region II to Region I.

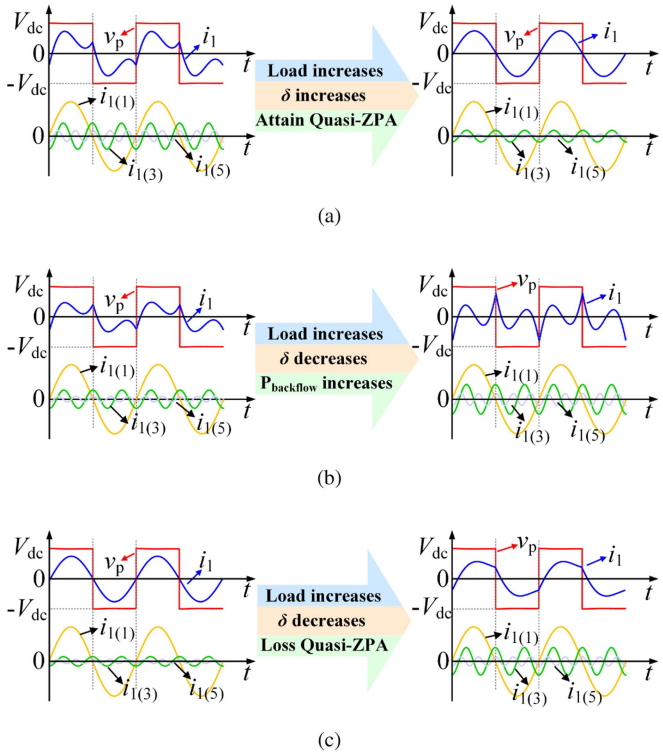

Fig. 7. Impact of δ on input current. (a) LCC-LCC topology. (b) LCL-S topology. (c) S-LCC topology.

III. Modulation Strategies for Bilateral LCC Under Multiple Working Conditions

A. Analysis on the Inductive Characteristics of the Full-Bridge Controlled Rectifier in the BPWT System

Fig. 8 illustrates the LCC-LCC topology. Due to load variations, excessive backflow power can result in reduced efficiency. Therefore, phase shift control is implemented to enable the topology to achieve constant power output and ZVS, thereby reducing power loss caused by backflow power in the system. During the period from t_0 to t_4, it can be determined that

$$\begin{cases} \omega t_1 &= \frac{\pi}{2} - \frac{\beta}{2} \\ \omega t_2 &= \frac{\pi}{2} + \frac{\beta}{2}. \end{cases} \tag{8}$$

The voltage of $V_{\rm s}$ is a three-level square wave. From t_0 to t_4, the Fourier expansions of $V_{\rm s}$, $i_{\rm p}$, and $i_{\rm s}$ can be calculated as follows:

$$V_{\rm s}(t) = \frac{4V_{\rm o}}{\pi} \sum_{n=1}^{k} \frac{1}{n} \cos\left(\frac{\pi}{2} + \frac{n\beta}{2}\right) \sin(n\omega t). \tag{9}$$

According to (9), the RMS value of the fundamental harmonic component of $V_{\rm s}$ is

$$V_{\rm s} = \frac{2\sqrt{2}}{\pi} V_{\rm o} \sin\frac{\beta}{2}. \tag{10}$$

According to the basic circuit theory, the input active power of the front-stage of the active rectifier is

$$P_{\rm s}(\beta, \varphi) = V_{\rm s} I_4 \cos(\varphi) = \frac{2\sqrt{2}}{\pi} V_{\rm o} I_4 \sin\frac{\beta}{2} \cos(\varphi). \tag{11}$$

According to (11), I_4 can be obtained, where $V_{\rm o}$ and $I_{\rm o}$ represent the voltage and current across the load

$$I_4 = \frac{\pi I_{\rm o}}{2\sqrt{2} \sin\frac{\beta}{2} \cos(\varphi)}. \tag{12}$$

According to (9), (10), (11), and (12), by regarding the active rectifier, the load resistor, and the filter capacitor as $Z_{\rm eq}$ for modeling, $Z_{\rm eq}$ can be calculated

$$Z_{\rm eq} = \frac{V_{\rm s}}{I_4} = R_{\rm eq} + jX_{\rm eq}. \tag{13}$$

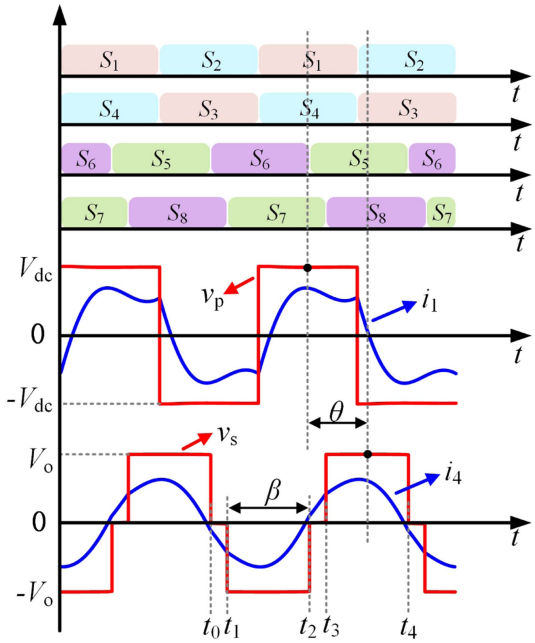

Fig. 8. Schematic diagram of the working waveform of primary-Side ZVS under Phase-Shift control.

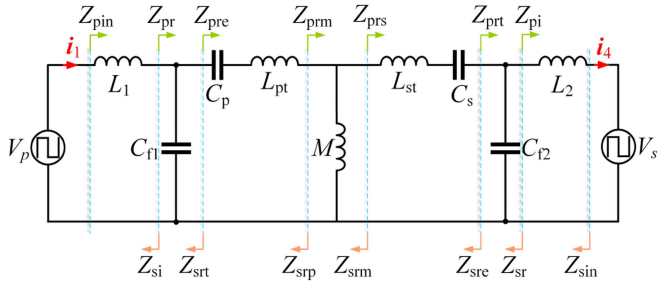

Fig. 9. Active rectifier circuit model.

Based on the relationship of the impedance triangle, R_{eq} and X_{eq} can be calculated, respectively, as follows:

$$\begin{cases} R_{eq} = \frac{8}{\pi^2} R \sin^2\left(\frac{\beta}{2}\right)\cos^2(\varphi) \\ X_{eq} = \frac{8}{\pi^2} R \sin^2\left(\frac{\beta}{2}\right)\cos(\varphi)\sin(\varphi). \end{cases} \tag{14}$$

B. Relationship Between the Output Power and Phase - Shift Angle in the BPWT System

Fig. 1 illustrates a typical BWPT system utilizing the LCC–LCC topology. The primary-side inverter receives electrical energy from the power grid via a bidirectional ac/dc converter and is powered by the direct current voltage V_{dc}. The secondary side is connected to the electric vehicle, supplying the battery load V_o to power the vehicle or harvest electrical energy. If the electric vehicle operates in the V2G state, the ac/dc converter regulates the grid current, enabling the vehicle to feed power back to the grid.

Fig. 9 presents the schematic diagram, which can be further simplified using impedance network analysis. When supplying power to the battery, the secondary side operates as a constant-voltage source. The circuit model of the BWPT system is depicted as shown. From the perspective of the primary side, the input impedance of each part is calculated as follows:

$$\begin{cases} Z_{pi(n)} = jn\omega L_2 \\ Z_{prt(n)} = \frac{Z_{pi(n)}}{jn\omega C_{f2} Z_{pi(n)}+1} \\ Z_{prs(n)} = Z_{prt(n)} + \frac{1}{jn\omega C_s} + jn\omega(L_p + M) \\ Z_{prm(n)} = \frac{jn\omega M Z_{prs(n)}}{jn\omega M + Z_{prs(n)}} \\ Z_{pre(n)} = Z_{prm(n)} + \frac{1}{jn\omega C_p} + jn\omega(L_p - M) \\ Z_{pr(n)} = \frac{Z_{pre(n)}}{jn\omega C_{f1} Z_{pre(n)}+1} \\ Z_{pin(n)} = Z_{pr(n)} + jn\omega L_1. \end{cases} \tag{15}$$

Calculated by looking from the secondary side, the input impedance of each part is as follows:

$$\begin{cases} Z_{si(n)} = jn\omega L_1 \\ Z_{srt(n)} = \frac{Z_{si(n)}}{jn\omega C_{f1} Z_{si(n)}+1} \\ Z_{srp(n)} = Z_{srt(n)} + \frac{1}{jn\omega C_p} + jn\omega(L_p - M) \\ Z_{srm(n)} = \frac{jn\omega M Z_{srp(n)}}{jn\omega M + Z_{srp(n)}} \\ Z_{sre(n)} = Z_{srm(n)} + \frac{1}{jn\omega C_s} + jn\omega(L_p + M) \\ Z_{sr(n)} = \frac{Z_{sre(n)}}{jn\omega C_{f2} Z_{sre(n)}+1} \\ Z_{sin(n)} = Z_{sr(n)} + jn\omega L_2. \end{cases} \tag{16}$$

The impedances Z_{ps} and Z_{sp} are derived from (15) and (16) as follows:

$$\begin{cases} Z_{ps(n)} = \frac{(Z_{si(n)}+Z_{pr(n)})Z_{pre(n)}Z_{prs(n)}Z_{pi(n)}}{Z_{pr(n)}Z_{prm(n)}Z_{prt(n)}} \\ Z_{sp(n)} = \frac{(Z_{pi(n)}+Z_{sr(n)})Z_{sre(n)}Z_{srp(n)}Z_{si(n)}}{Z_{sr(n)}Z_{srm(n)}Z_{srt(n)}}. \end{cases} \tag{17}$$

From (9) and (17), the harmonic order and the output power P_o of the system are derived as

$$P_o = \mathrm{Re}\left\{\sum_{n=1,3,\ldots}^{\infty}\left(\frac{V_{s(n)}^2}{Z_{sin(n)}} + \frac{V_{p(n)}V_{s(n)}}{Z_{ps(n)}}\right)\right\}$$

$$= \frac{8MV_{dc}V_o}{\pi^2 L_1 L_2 \omega}\sum_{n=1,3,\ldots}^{\infty}\left\{\frac{1}{n^2}\left[\cos^2\left(\frac{\pi}{2}+\frac{n\beta}{2}\right)\sin^2(n\omega t)\sin\theta\right]\right\}. \tag{18}$$

Among them, n represents the harmonic order of the Fourier decomposition of the input voltage source, k is the coupling coefficient of the energy transfer coil, β is the secondary-side phase shift angle of the system, that is, the pulsewidth angle of the secondary-side square wave voltage, and θ is the external phase shift angle of the system.

It can be seen from (18) that the stability of the system's output power can be maintained by adjusting the internal phase

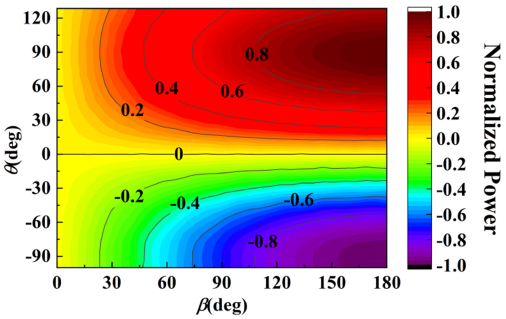

Fig. 10. Relationship between the normalized output power of the system and the phase shift angle.

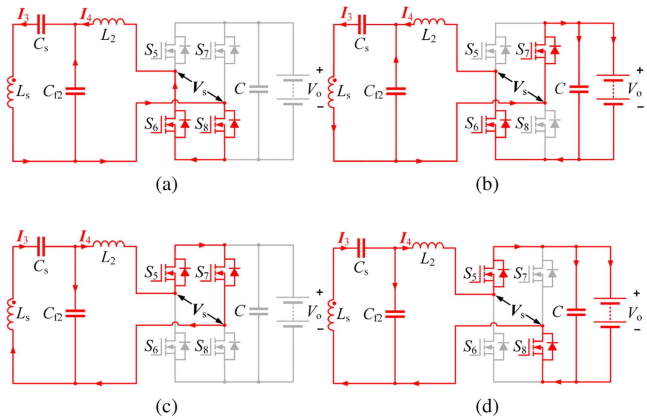

Fig. 11. Working modes of the BWPT system. (a) $t_0 - t_1$. (b) $t_1 - t_2$. (c) $t_2 - t_3$. (d) $t_3 - t_4$.

shift angle β or the external phase shift angle θ. When the external phase shift angle θ is within the range of $(0°, 180°)$, the transmission power is positive and the energy is transferred from the primary side to the secondary side; when θ is within the range of $(-180°, 0°)$, the transmission power is negative and the energy is transferred from the secondary side to the primary side. Therefore, the external phase shift angle θ can take any value within the range of $(0°, 180°)$ to adjust the forward output power.

In Fig. 10, the output power is normalized and its relationship with the internal phase shift angle β or the external phase shift angle θ is plotted. It can be seen that when $\theta = \pm 90°$, the maximum power in the forward and reverse directions can be obtained, respectively.

C. Analysis of the System Operating Modes

According to (18), a full-bridge active rectification system is used to achieve constant power output over a wide load range. The active control capability of the active rectifier devices overcomes the limitation that traditional passive rectification cannot dynamically adjust power output with varying loads, and by dynamically adjusting the phase angle of the secondary side, constant power output and ZVS is achieved over a wide load range. Fig. 8 shows the circuit waveform of the full-bridge active rectifier module in the WPT system, and Fig. 11(a)–(d) present the working mode analysis of the full-bridge active rectifier bridge.

Mode 1 ($t_0 < t < t_1$): During this interval, switches S_6 and S_8 of the active rectifier bridge are turned on. The circuit waveforms are shown in Fig. 8, where the current i_4 flows through S_6 and S_8 in the converter depicted in Fig. 11(a) during this period, while Vs remains at the 0-level.

Mode 2 ($t_1 < t < t_2$): As illustrated in Fig. 11(b), the current flows through the active rectifier bridge S_6 and S_7, with the resonant current increasing initially and subsequently decreasing during this interval. The voltage V_s remains at $-V_o$ level.

Mode 3 ($t_2 < t < t_3$): As depicted in Fig. 11(c), in this mode, the current flows through switches S_5 and S_7 of the active rectifier bridge, while V_s remains at the 0-level, and the current waveform is illustrated in Fig. 8.

Mode 4 ($t_3 < t < t_4$): As seen in Fig. 11(d), within this time interval, the current begins to flow in the positive direction through switches S_5 and S_8 of the active rectifier. The current value gradually increases and then decreases, with V_s remaining at the $+V_o$ level.

To enhance understanding, Fig. 12 presents the overall process, the use of the impedance factor δ during the pre-experimental stage to guide parameter selection, followed by the implementation of wide-load constant power control in the control phase.

IV. Simulation Analysis

A simulation model is built to verify the theoretical formulas. All models utilize the FHA to calculate the parameters of each component. The switching frequency of the input voltage is 85 kHz. Theoretical calculations of δ are conducted for six different topologies, and the simulation results are shown in Fig. 13(a)–(f). In Fig. 13(a)–(c), $\delta < \delta_{\text{th}}$ with theoretical values of 1.15, 1.98, and 1.66, respectively; under these conditions, the system operates with ZVS but cannot achieve quasi-ZPA. In contrast, in Fig. 13(d)–(f), $\delta > \delta_{\text{th}}$ with theoretical values of 2.4, 4.34, and 2.71, respectively. In these cases, the input current waveform is dominated by the fundamental harmonic component, and the influence of harmonics is minimal. Moreover, the full-bridge inverter, filter capacitor, and load in the system, when equivalent to the input impedance terminal, will present inductive characteristics. Therefore, the waveforms from (a) to (f) will all present weak inductive characteristics, and the specific inductance value is related to the resonant topology. Previous analysis has also addressed this phenomenon. However, based on the results of simulations, the inductive effect is not significant and only adds a slight inductive characteristic to the system. The simulation results are consistent with the theoretical analysis in Fig. 6.

V. Experimental Verification

The commonly used SS, LCC-S, and LCC–LCC topologies were selected for experimental validation, as shown in Fig. 14, where the microprocessor TMS320F28335 serves as the control core. The simulation and experimental prototype parameters are

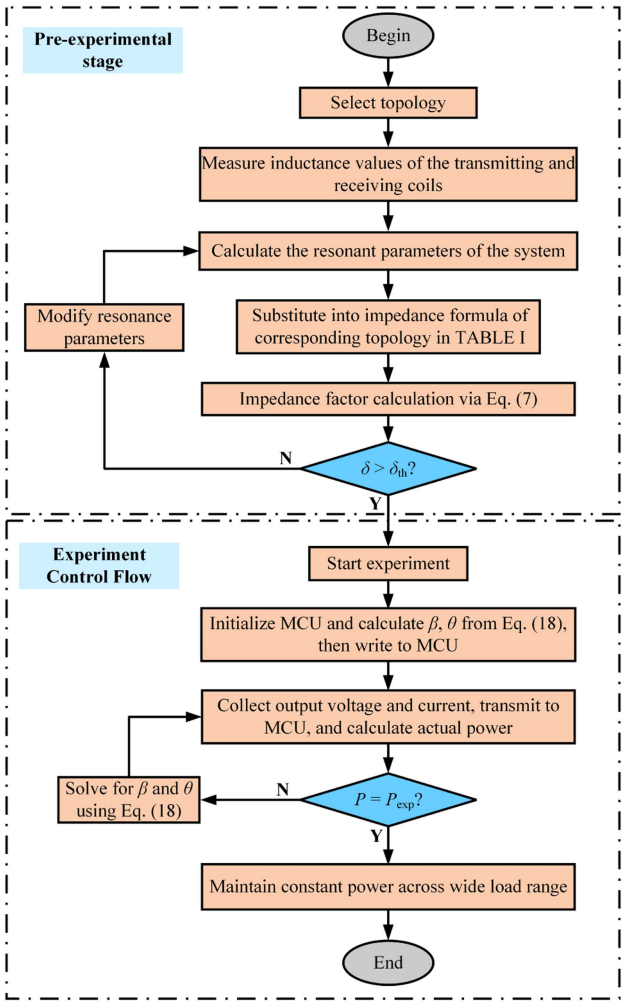

Fig. 12. Overall system design flowchart.

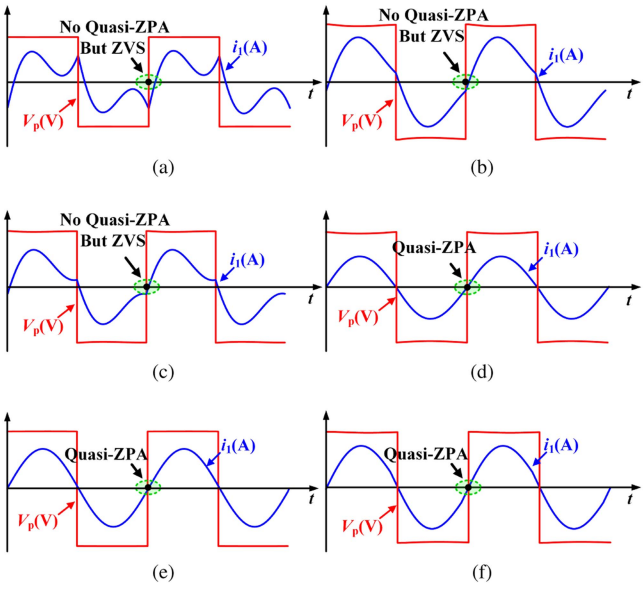

Fig. 13. Simulation waveforms of different topologies under the traditional ZPA tuning scheme. (a) LCL-S topology. (b) LCC-S topology. (c) LCC–LCC topology. (d) SS topology. (e) S-LCL topology. (f) S-LCC topology.

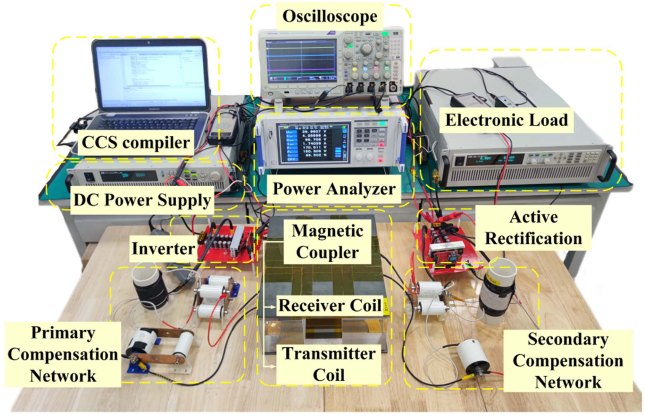

Fig. 14. Experimental platform of the WPT system.

TABLE II
KEY PARAMETERS OF THE WPT PROTOTYPE

Items	Primary Side	Second Side
LCC Topology	L_1=23.08 μH	L_2= 22.23 μH
	L_p=141.2 μH	L_s=139.9 μH
	C_{f1}=153.4 nF	C_{f2} 164.4 nF
	C_p=29.67 nF	C_s=29.8 nF
S Topology	L_p=141.2 μH	L_s=139.9 μH
	C_p=24.27 nF	C_s=25.41 nF
LCL Topology	L_1=141.2 μH	L_2=139.9 μH
	L_p=138.6 μH	L_s=136.1 μH
	C_p=24.27 nF	C_s=25.41 nF
MOSFETs	IPW60R060P7	
Input voltage	V_{dc}=40 V	
Coupling coefficient	k=0.183	
Resonant frequency	f_s=85 kHz	
Load resistance	R=5–60 Ω	

listed in Table II. The Tektronix MDO3024 precision digital oscilloscope was employed for voltage and current measurements, and the HIOKI PW6001 high-precision power analyzer was used for power efficiency measurements.

A. *Waveforms of Quasi-ZPA and ZVS*

Fig. 15 presents the experimental waveforms of three resonant topologies: SS, LCC-S, and LCC–LCC. After determining the resonant parameters of each topology using FHA, the input current waveform characteristics are observed for different load conditions, which correspond to different values of δ. For the SS topology, when $R = 10\ \Omega$, the calculated value of δ is 2.39, which satisfies the condition $\delta > 0.95\delta_{th}$, indicating that the system can achieve quasi-ZPA. According to the variation trend of the SS topology curve in Fig. 6, δ increases with increasing load. Consequently, for $R = 30\ \Omega$ and $R = 50\ \Omega$, the corresponding δ values are 2.86 and 3.08, respectively. Throughout this range, δ consistently remains above $0.95\delta_{th}$, ensuring that both quasi-ZPA and ZVS are maintained in the system. For the LCC-S topology, when $R = 10\ \Omega$, δ is calculated to be 1.94,

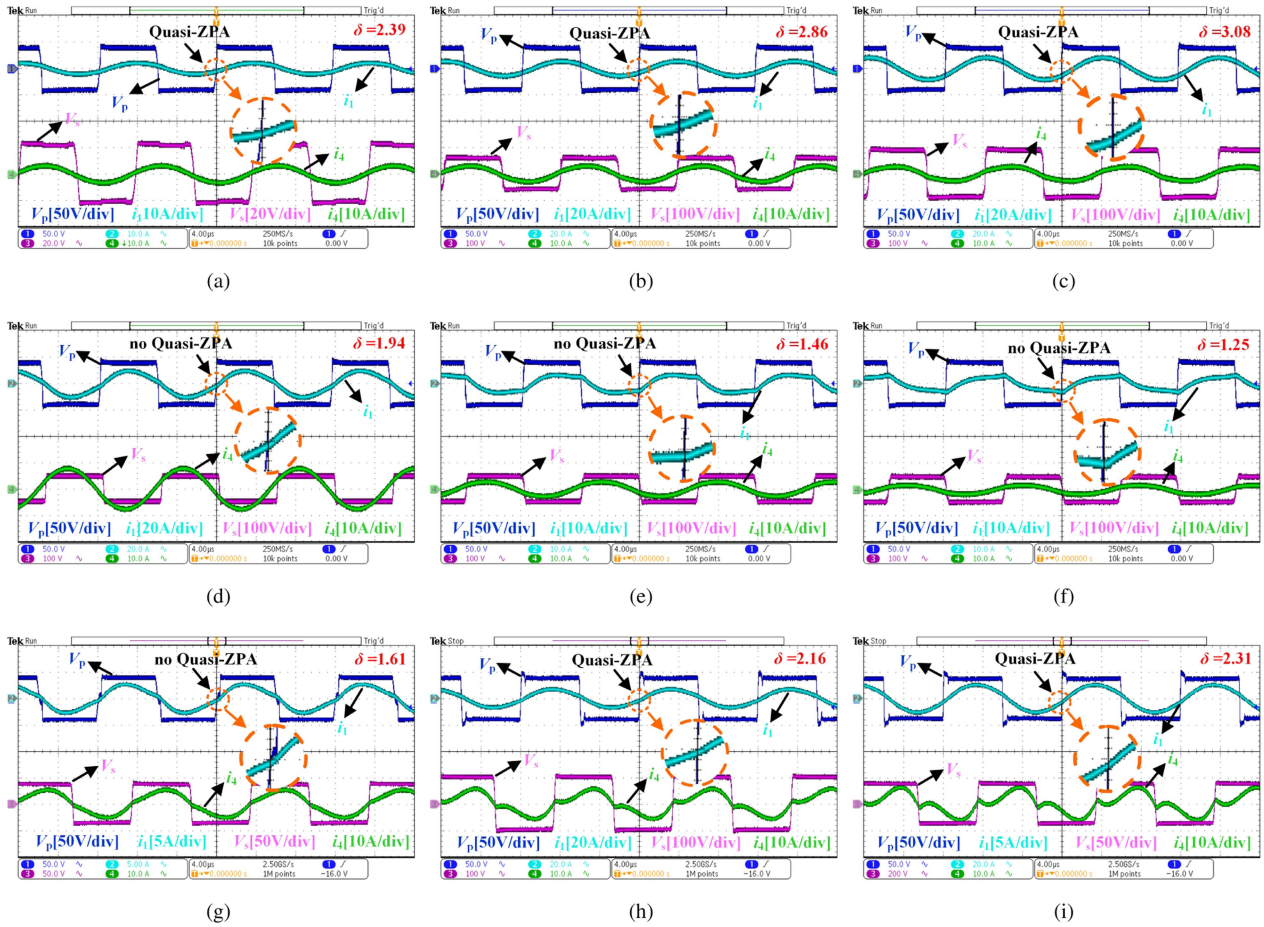

Fig. 15. Experimental waveforms of different topologies under the fundamental harmonic analysis parameter scheme. (a) SS topology with $R = 10\ \Omega$. (b) SS topology with $R = 30\ \Omega$. (c) SS topology with $R = 50\ \Omega$. (d) LCC-S topology with $R = 10\ \Omega$. (e) LCC-S topology with $R = 30\ \Omega$. (f) LCC-S topology with $R = 50\ \Omega$. (g) LCC–LCC topology with $R = 10\ \Omega$. (h) LCC–LCC topology with $R = 30\ \Omega$. (i) LCC–LCC topology with $R = 50\ \Omega$.

which is less than $0.95\delta_{\text{th}}$, indicating that the system cannot achieve quasi-ZPA. It is observed that, at the instant when the voltage V_{p} exhibits a step change, the waveform is slightly influenced by harmonics; however, this influence is minimal and the system operates near the quasi-ZPA condition. According to the variation trend of the LCC-S topology curve in Fig. 6, δ further decreases as the load increases. For $R = 30\ \Omega$ and $R = 50\ \Omega$, the corresponding δ values are 1.46 and 1.25, respectively, and the criterion $\delta < 0.95\delta_{\text{th}}$ is still satisfied, indicating that quasi-ZPA remains unattainable.

Moreover, as δ continues to decrease and deviates further from δ_{th}, the influence of harmonics becomes increasingly significant, such that only ZVS can be maintained in the system. For the LCC–LCC topology, when $R = 10\ \Omega$, the calculated value of δ is 1.61, which is less than $0.95\delta_{\text{th}}$, indicating that the system cannot achieve quasi-ZPA under these conditions. According to the variation trend of the LCC–LCC topology curve in Fig. 6, δ increases with increasing load. Therefore, for $R = 30\ \Omega$ and $R = 50\ \Omega$, the corresponding δ values rise to 2.16 and 2.31, respectively. In these cases, δ exceeds $0.95\delta_{\text{th}}$, and the input current waveform becomes progressively dominated by its fundamental harmonic component, thereby enabling the system to achieve both quasi-ZPA and ZVS. A comprehensive summary of the relationship among R, δ, and the input current conditions for all considered topologies is provided in Table III.

TABLE III
REALIZATION OF QUASI-ZPA IN DIFFERENT TOPOLOGIES AND LOAD CONDITIONS

Topology	$R(\Omega)$	δ	Quasi-ZPA
SS	10	2.39	✓
	30	2.86	✓
	50	3.08	✓
LCC-S	10	1.94	✗
	30	1.46	✗
	50	1.25	✗
LCC-LCC	10	1.61	✗
	30	2.16	✓
	50	2.31	✓

B. Optimization of ZVS Under Load Variations Through Phase Shift Modulation

As shown in Fig. 16, when the load changes from 14 to 50 Ω, the system's backflow power varies accordingly. Within an appropriate range, changes in backflow power can effectively

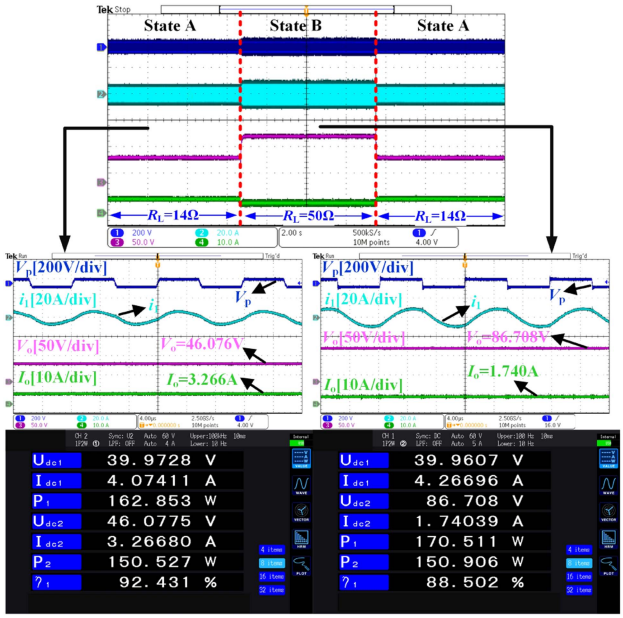

Fig. 16. Constant power efficiency improvement experiment for LCC–LCC topology with load varying from 14 to 50 Ω and back to 14 Ω.

achieve optimal ZVS. However, under complex working conditions, the uncertainty of load variations causes uncontrollable fluctuations in backflow power, leading to increased losses. Therefore, instantaneous internal and external phase shift angle modulation should be implemented on the secondary side when the load changes, ensuring stable power output and improved efficiency.

VI. Conclusion

Comprehensive analysis of the relationships among ZVS, ZPA, and quasi-ZPA in WPT systems has been presented in this article. The phenomenon of some topologies achieving ZVS in the time domain due to harmonic influence, despite being configured with ZPA resonant parameters under FHA, is discussed. Importantly, an impedance factor δ method is proposed to investigate the ZVS and quasi-ZPA phenomena in WPT systems under different topologies and load values. The relationship between δ and quasi-ZPA is established in this article, and the boundary value required to achieve quasi-ZPA is defined as δ_{th}. To verify the effectiveness of the analysis, a 1 kW/85 kHz experimental prototype is constructed. Experimental results show that the variation of the impedance factor δ can accurately predict the input current characteristics of the WPT system. Moreover, the comparison between δ and the threshold δ_{th} enables a pre-experimental assessment of whether the system can achieve quasi-ZPA. When δ exceeds $0.95\delta_{\text{th}}$, the system achieves quasi-ZPA. Below this threshold, the system loses quasi-ZPA, with the effect of harmonics becoming more pronounced. In addition, phase shift control can maintain constant power output and ZVS over a wide load range. A more detailed phase shift control strategy will be investigated in future work. The system also achieves a peak efficiency of approximately 92%.

References

[1] Z. Zhang, H. Pang, A. Georgiadis, and C. Cecati, "Wireless power transfer—an overview," *IEEE Trans. Ind. Electron.*, vol. 66, no. 2, pp. 1044–1058, Feb. 2019.

[2] S. Roy, A. N. M. W. Azad, S. Baidya, M. K. Alam, and F. Khan, "Powering solutions for biomedical sensors and implants inside the human body: A comprehensive review on energy harvesting units, energy storage, and wireless power transfer techniques," *IEEE Trans. Power Electron.*, vol. 37, no. 10, pp. 12237–12263, Oct. 2022.

[3] X. Li et al., "A dual-coupled double-LCC system with the capability of misalignment tolerance improvement for wireless charging substation inspection robots," *IEEE Trans. Power Electron.*, vol. 39, no. 6, pp. 6624–6629, Jun. 2024.

[4] Y. Cho, A. Basir, Y.-H. Lim, and H. Yoo, "Influence of heterogeneous human body on midfield wireless power transfer for implantable heart devices," *IEEE Trans. Microw. Theory Techn.*, vol. 72, no. 3, pp. 2009–2018, Mar. 2024.

[5] I. A. Shah, M. Zada, S. A. A. Shah, A. Basir, and H. Yoo, "Flexible metasurface-coupled efficient wireless power transfer system for implantable devices," *IEEE Trans. Microw. Theory Techn.*, vol. 72, no. 4, pp. 2534–2547, Apr. 2024.

[6] Z. Chen, X. Zhang, F. Xu, M. Li, Z. Yuan, and Q. Yang, "Wide rotation-misalignment-tolerance design of magnetic coupled structure for AUVs wireless charging system," *IEEE Trans. Ind. Electron.*, vol. 71, no. 11, pp. 14086–14096, Nov. 2024.

[7] V.-B. Vu, D.-H. Tran, and W. Choi, "Implementation of the constant current and constant voltage charge of inductive power transfer systems with the double-sided LCC compensation topology for electric vehicle battery charge applications," *IEEE Trans. Power Electron.*, vol. 33, no. 9, pp. 7398–7410, Sep. 2018.

[8] S. Nie, W. Han, Z. Luo, C. Perera, and P. W. Lehn, "Sequential mutual-inductance identification method for wireless power transfer systems of electric vehicles," *IEEE Trans. Transp. Electrific.*, vol. 10, no. 3, pp. 5178–5189, Sep. 2024.

[9] X. Zhang, R. Xue, F. Wang, F. Xu, T. Chen, and Z. Chen, "Capacitor tuning of LCC-LCC compensated IPT system with constant-power output and large misalignments tolerance for electric vehicles," *IEEE Trans. Power Electron.*, vol. 38, no. 10, pp. 11928–11939, Oct. 2023.

[10] Y. Jiang, J. Liu, X. Hu, L. Wang, Y. Wang, and G. Ning, "An optimized frequency and phase shift control strategy for constant current charging and zero voltage switching operation in series-series compensated wireless power transmission," in *Proc. IEEE Energy Convers. Congr. Expo.*, Cincinnati, OH, USA, Oct. 2017, pp. 961–966.

[11] Z. Huang, S.-C. Wong, and C. K. Tse, "Control design for optimizing efficiency in inductive power transfer systems," *IEEE Trans. Power Electron.*, vol. 33, no. 5, pp. 4523–4534, May 2018.

[12] W. Zhong and S. Y. R. Hui, "Maximum energy efficiency operation of series-series resonant wireless power transfer systems using on-off keying modulation," *IEEE Trans. Power Electron.*, vol. 33, no. 4, pp. 3595–3603, Apr. 2018.

[13] R. L. Steigerwald, "A comparison of half-bridge resonant converter topologies," *IEEE Trans. Power Electron.*, vol. 3, no. 2, pp. 174–182, Apr. 1988.

[14] W. X. Zhong and S. Y. R. Hui, "Maximum energy efficiency tracking for wireless power transfer systems," *IEEE Trans. Power Electron.*, vol. 30, no. 7, pp. 4025–4034, Jul. 2015.

[15] L. Yang et al., "A high-efficiency integrated LCC/S WPT system with constant current output," *IEEE J. Emerg. Sel. Topics Power Electron.*, vol. 12, no. 1, pp. 341–354, Feb. 2024.

[16] Y. Guo, Y. Zhang, W. Zhang, and L. Wang, "Battery parameter identification based on wireless power transfer system with rectifier load," *IEEE Trans. Ind. Electron.*, vol. 68, no. 8, pp. 6893–6904, Aug. 2021.

[17] Y. Guo, Y. Zhang, S. Li, C. Tao, and L. Wang, "Load parameter joint identification of wireless power transfer system based on the DC input current and phase-shift angle," *IEEE Trans. Power Electron.*, vol. 35, no. 10, pp. 10542–10553, Oct. 2020.

[18] Y. Guo, L. Wang, Y. Zhang, S. Li, and C. Liao, "Rectifier load analysis for electric vehicle wireless charging system," *IEEE Trans. Ind. Electron.*, vol. 65, no. 9, pp. 6970–6982, Sep. 2018.

[19] A. Berger, M. Agostinelli, S. Vesti, J. A. Oliver, J. A. Cobos, and M. Huemer, "A wireless charging system applying phase-shift and amplitude control to maximize efficiency and extractable power," *IEEE Trans. Power Electron.*, vol. 30, no. 11, pp. 6338–6348, Nov. 2015.

[20] K. Colak, E. Asa, M. Bojarski, D. Czarkowski, and O. C. Onar, "A novel phase-shift control of semibridgeless active rectifier for wireless power transfer," *IEEE Trans. Power Electron.*, vol. 30, no. 11, pp. 6288–6297, Nov. 2015.
[21] S. Li, W. Li, J. Deng, T. D. Nguyen, and C. C. Mi, "A double-sided LCC compensation network and its tuning method for wireless power transfer," *IEEE Trans. Veh. Technol.*, vol. 64, no. 6, pp. 2261–2273, Jun. 2015.
[22] F. Xu, S.-C. Wong, and C. K. Tse, "Inductive power transfer system with maximum efficiency tracking control and real-time mutual inductance estimation," *IEEE Trans. Power Electron.*, vol. 37, no. 5, pp. 6156–6167, May 2022.
[23] Y. Jia, L. Zhao, Z. Wang, C. Tang, F. Chen, and H. Feng, "Integrated LCC-LCC topology for WPT system with CC output regarding air gap and load variations," *IEEE Trans. Power Electron.*, vol. 39, no. 10, pp. 11904–11915, Oct. 2024.
[24] G. Zhu, J. Dong, W. Shi, T. B. Soeiro, J. Xu, and P. Bauer, "A mode-switching-based phase shift control for optimized efficiency and wide ZVS operations in wireless power transfer systems," *IEEE Trans. Power Electron.*, vol. 38, no. 4, pp. 5561–5575, Apr. 2023, doi: 10.1109/TPEL.2022.3231451.
[25] J. Zeng et al., "A fast front-end monitoring method for mutual inductance and load movement in SS-compensated wireless power transfer systems based on harmonics extraction," *IEEE Trans. Power Electron.*, vol. 40, no. 1, pp. 2569–2580, Jan. 2025.
[26] H. H. Wu, A. Gilchrist, K. Sealy, and D. Bronson, "A 90 percent efficient 5 kW inductive charger for EVs," in *Proc. IEEE Energy Convers. Congr. Expo.*, 2012, pp. 275–282.
[27] V. Yenil and S. Cetin, "An improved pulse density modulation control for secondary side controlled wireless power transfer system using LCC-S compensation," *IEEE Trans. Ind. Electron.*, vol. 69, no. 12, pp. 12762–12772, Dec. 2022.
[28] R. Mai, Y. Chen, Y. Zhang, N. Yang, G. Cao, and Z. He, "Optimization of the passive components for an S-LCC topology-based WPT system for charging massive electric bicycles," *IEEE Trans. Ind. Electron.*, vol. 65, no. 7, pp. 5497–5508, Jul. 2018.
[29] H. Namiki, T. Imura, and Y. Hori, "Magnetic field resonant coupling in wireless power transfer: Comparison of multiple circuits using LCL," in *Proc. IEEE 7th Southern Power Electron. Conf.*, 2022, pp. 1–6.

Xian Zhang received the M.E. and Ph.D. degrees in electrical engineering from the Hebei University of Technology, Tianjin, China, in 2009 and 2012, respectively.

He is currently a Professor with the Hebei University of Technology. He is the Director of the China Electrotechnical Society and the Secretary-General of the National Specialized Committee on Wireless Power Transmission Technology. His research interests encompass intelligent high power wireless power transmission technology, measurement of 3-D electromagnetic fields, and numerical calculations of modern engineering electromagnetic fields.

Zhenlei Zhang received the B.S. degree in electronic science and technology from the Tianjin University of Technology and Education, Tianjin, China, in 2022. He is currently working toward the M.S. degree in electrical engineering with the Hebei University of Technology, Tianjin, China.

His current research interests include wireless power transfer, modulation and control techniques, and their applications in industry.

Fei Xu (Member, IEEE) received the B.Eng. degree from China Agricultural University, Beijing, China, in 2016, the M.Phil. degree from the Institute of Electrical Engineering, Chinese Academy of Sciences, Beijing, China, in 2019, both in electrical engineering, and the Ph.D. degree in power electronics from The Hong Kong Polytechnic University, Hong Kong, 2022.

He is currently an Assistant Professor with the Department of Electrical Engineering and State Key Laboratory of Reliability and Intelligence of Electrical Equipment, Hebei University of Technology, Tianjin, China. His research interests include wireless power transfer, power electronic, and electric vehicles.

Zhixin Chen (Graduate Student Member, IEEE) received the B.S. degree in electrical engineering and automation from the Liren College of Yanshan University, Qinhuang-dao, China, in 2018, and the M.S. degree in electrical engineering from the Tiangong University, Tianjin, China, in 2022. He is currently working toward the Ph.D. degree in electrical engineering with the Hebei University of Technology, Tianjin.

His current research interests include wireless power transfer, and its industrial applications.